![Aalto University]

Smyl, Danny; Antin, Kim-Niklas; Liu, Dong; Bossuyt, Sven

Coupled Digital Image Correlation and Quasi-Static Elasticity Imaging of inhomogeneous orthotropic composite structures

Coupled Digital Image Correlation and Quasi-Static Elasticity Imaging of inhomogeneous orthotropic composite structures

Danny Smyl[1]

[1]Department of Mechanical Engineering, Aalto University, Espoo, Finland

E-mail: `danny.smyl@aalto.fi`

Kim-Niklas Antin[1]

Dong Liu[2,3,4]

[2]CAS Key Laboratory of Microscale Magnetic Resonance and Department of Modern Physics, University of Science and Technology of China (USTC), Hefei 230026, China
[3]Hefei National Laboratory for Physical Sciences at the Microscale, USTC, China
[4]Synergetic Innovation Center of Quantum Information and Quantum Physics, USTC, China

E-mail: `dong2016@ustc.edu.cn`

Sven Bossuyt[1]

Abstract. The ability to accurately determine elastic properties of orthotropic materials is important in the design and health assessment of composite structures. Direct methods using strain gauges and extensometers for estimating orthotropic properties have become popular in recent years. In cases where strains are highly localized, the material properties are inhomogeneous, or the material has localized damage, the use of these measurement schemes often provides insufficient information. To address this, we propose an inverse method, based on Quasi-Static Elasticity Imaging (QSEI) for determining inhomogeneous orthotropic elastic properties using distributed displacement measurements obtained from Digital Image Correlation (DIC). The QSEI-based approach is first tested with simulated noisy displacement data considering in-plane deformations of plate geometries undergoing stretching and bending. Following, experimental DIC measurements are applied to test the feasibility of the QSEI-based approach. Elastic properties of uni-directional CFRP beams with and without localized damage are estimated using the proposed approach. Results demonstrate the feasibility of the proposed inverse approach.

1. Introduction

Experimentally estimating elastic properties of composite materials is challenging due to the materials' orthotropy [1], requiring the estimation of four or more coefficients [2]. It is then no surprise that orthotropic elastic properties, such as Poisson ratios, elastic moduli, and shear modulus, are often determined using analytical or numerical modeling [3–5]. In cases where using such models results in unacceptable uncertainty (e.g. characterizing novel materials), hybrid experimental-numerical approaches are commonly employed. Owing to their simplicity, the use of direct methods, employing strain gauges and extensometers are often used for determining orthotropic properties [6–8]. However, these methods are limited, in that, the measurement devices only offer point information averaged over the length of the gauge. For composite structures with highly localized strains, inhomogenity in material properties, or localized damage, direct methods often offer insufficient information. For this reason, employment of methods using full-field measurements, such as guided/lamb waves [9–11], electrical methods [12] and Digital Image Correlation (DIC) [13–16] have recently become popular.

The use of distributed measurement systems coupled with computational inverse regimes have been successful in determining orthotropic elastic properties assumed to be homogeneously distributed. Possibly the first efforts to determine such properties utilized modal analysis and early implementations of the Finite Element Method, representative works include [17–19]. Later, developments using Bayesian [20] and superposition-based [21] approaches showed notable improvements in accuracy. These methods were based on Kirchhoff's theory of thin plates, and therefore neglected the influence of the shear modulus. In more recent years, researchers have proposed regimes for computing all the homogeneous orthotropic elastic properties, including the shear modulus, using a multitude of approaches, for example, by using flexural resonance frequencies of beams [22, 23], neural networks [24], and mixed full-field methods [25–27].

In the light of the significant successes of these works, few regimes exist to reconstruct (estimate, using an inverse method) highly inhomogeneous distributions of *orthotropic* elastic properties which may result from, for example, mechanical damage, environmental degradation, or manufacturing errors. Inspired by the recent advances utilizing full-field measurements to characterize composite materials, we propose an inverse algorithm for estimating inhomgeneously-distributed orthotropic elastic properties for composite structures in plane-stress using DIC measurements. The approach proposed herein is similar to those used by researchers in the field of inverse problems, such as in "two-step" applications of Quantitative Photoacoustic Tomography [28, 29].

The proposed inverse algorithm is rooted in concepts of Quasi-Static Elasticity Imaging (QSEI), which aims to determine inhomogeneous elastic moduli using quasi-static displacement fields. While applications of QSEI in structural applications are scarce (cf. [30–32] for closely-related approaches), QSEI is well developed in medical applications, e.g. to image tissue abnormalities [33–37]. In this work, we utilize concepts in QSEI

and stacked approaches for simultaneous inverse estimation of multiple unknown distributed parameter fields [38, 39]. Specifically, we propose a framework for simultaneous estimation of inhomogeneous orthotropic elastic properties by employing a stacking method using constrained least-squares optimization.

This article is organized as follows. First, we describe estimated parameters using the proposed scheme. After, we describe the inverse problem, the solution to the inverse problem, and the DIC approach used to obtain experimental displacement fields. Following, we test the QSEI algorithm using simulated displacement data for in-plane plate stretching and bending. We then use experimental displacement measurements obtained using DIC to test the feasibility of the scheme for imaging uni-directional carbon fiber reinforced polymer (CFRP) beams with and without localized damage. Finally, discussion and conclusions are presented.

2. Determining orthotropic elastic properties using QSEI

2.1. Estimation parameters

In this work, we study 2-D othotropic geometries neglecting out-of-plane deformations. For simplicity, we assume the geometry has uni-directional fiber orientation in the longitudinal direction (x-direction), denoted by the subscript "1." The transverse direction (y-direction) is denoted with the subscript "2." Based off these preliminaries, the orthotropic properties we are required to estimate are given by the constitutive stress-strain ($\sigma - \epsilon$) relation for plane stress [40]:

$$
\underbrace{\begin{bmatrix} \sigma_1 \\ \sigma_2 \\ \sigma_{12} \end{bmatrix}}_{\sigma} = \underbrace{\begin{bmatrix} \frac{E_1}{1-\nu_{12}\nu_{21}} & \frac{\nu_{21}E_1}{1-\nu_{12}\nu_{21}} & 0 \\ \frac{\nu_{12}E_2}{1-\nu_{12}\nu_{21}} & \frac{E_2}{1-\nu_{12}\nu_{21}} & 0 \\ 0 & 0 & G_{12} \end{bmatrix}}_{\mathcal{C}} \underbrace{\begin{bmatrix} \epsilon_1 \\ \epsilon_2 \\ 2\epsilon_{12} \end{bmatrix}}_{\epsilon} \tag{1}
$$

where E_1 and E_2 are the elastic moduli, ν_{12} and ν_{21} are the Poisson ratios, G_{12} is shear modulus, and $\mathcal{C}$ is the stiffness matrix. From Eq. 1, it is apparent that five elastic properties need to be estimated.

2.2. Defining the inverse problem

The inverse problem is stated as follows. Given the 2D domain $\Omega(x, y)$, boundary information $\partial\Omega(x, y)$, measured displacement field u_m, and external forces F: determine the parameter field $\chi = [E_1(x, y), E_2(x, y), \nu_{12}(x, y), \nu_{21}(x, y), G_{12}(x, y)]^T$. Assuming a Gaussian noise model, the observation model for the inverse problem has the form

$$
u_m = U(\chi) + e \tag{2}
$$

where $U(\chi)$ are the simulated displacements and e is the Gaussian-distributed noise. To compute the simulated displacement field, $U(\chi)$, we employ the Finite Element Method. This is done using piece-wise linear triangular elements assuming incompressible plane-stress conditions. The forward model is written as

$$U_j = \sum_{i=1}^{N_n} K(\chi)_{ji}^{-1} F_i \tag{3}$$

where N_n is the total number of unknown displacements and $K(\chi)_{ji}^{-1}$ and F_i are the compliance matrix and force vector, respectively [36, 41].

The reconstruction problem, estimating χ from u_m, is ill-posed. This means that at least one of the well-posedness criteria (uniqueness, stability, and existence) does not hold. Practically speaking, the ill-posedness of estimating χ from u_m results in solutions that are sensitive to measurement noise, modeling errors, and outlier data [42, 43]. Due to the ill-posedness of this problem, we employ regularization in the constrained least-squares (LS) minimization problem, which is written as

$$\ell_\chi = \arg \min_{\substack{E_1 > E_2 \\ E_2 > 0 \\ G > 0 \\ 0 < \nu_{12} < 0.5}} \{||L_e(u_m - U(\chi))||^2 + \mathcal{R}_\chi(\chi)\} \tag{4}$$

where $\mathcal{R}_\chi$ is a compound regularization functional, L_e is a square triangular matrix computed as the Cholesky factor of the inverted noise covariances W^{-1} (i.e. $L_e^T L_e = W^{-1}$), and $|| \cdot ||$ denotes the Euclidean norm. The constraints shown on E_2, G_{12} and ν_{12} in Eq. 4 are required for physically-realistic solutions of χ based on known ranges for similar unidirectional CFRP materials [5]. The constraint $E_1 > E_2$ is related to prior knowledge of fiber orientation. These constraints were handled using cubic polynomial barrier functions.

In this paper, our method of regularization assumes that unknown parameters or material properties may be modeled using smooth distributions of χ. While sparsity-promoting regularization methods‡ may be used for estimating damage locations in materials with relatively homogeneous backgrounds, they are not appropriate for cases with large fluctuations in background distributions. Based on this realization, we select smoothness promoting regularization of the form:

$$\mathcal{R}_\chi = ||L_\chi(\chi - \chi_{\exp})||^2 \tag{5}$$

where $\chi_{\exp}$ is the homogeneous five-parameter solution computed by solving: $\chi_{\exp} = \min ||(u_m - U(E_1, E_2, \nu_{12}, \nu_{21}, G_{12})||^2$. In vectorized form, $\chi_{\exp}$ compiles the five expected values, i.e. $\chi_{\exp} = [E_{1,\exp}, E_{2,\exp}, \nu_{12,\exp}, \nu_{21,\exp}, G_{12,\exp}]^T$ where the shorthand "exp" is used in the lower right hand subscript to denote that it is an expected value for a given elastic property. Further, L_χ is a spatially-weighted matrix for each estimated material property

‡ For example, by employing the Total Variation functional [44, 45].

(for example, $\mathcal{R}_{E_1} = ||L_{E_1}(E_1 - E_{1,\text{exp}})||^2$). Here, we would like to add some specific remarks regarding the regularization used in this work:

- We may compute L_χ using the Cholesky factor of the inverted prior covariance matrix Γ_χ (i.e. $\Gamma_\chi^{-1} = L_\chi^T L_\chi$§), where the covariance matrix element (i,j) for a distributed parameter ω at locations x_i and x_j is given by

$$\Gamma_\omega(i,j) = a \exp\left(-\frac{||x_i - x_j||^2}{2b}\right) + c\delta_{ij} \tag{6}$$

  where a, b, and c are positive scalars and δ_{ij} is the Kronecker delta function.
- $\mathcal{R}_\chi$ and Γ_χ are important components of the inverse problem, as they incorporate prior information in the solution of Eq. 4 and significantly impact the behavior during iterative minimization described in the following section.
- The use of spatially-weighted regularization, as adopted herein, is not common in applications of QSEI. However, as demonstrated in [47], the contrast of reconstructed images has improved from the use of utilizing spatially-weighted regularization.

2.3. Solving the inverse problem

The QSEI problem is solved iteratively using a Gauss-Newton (GN) approach to update the solution of χ at each iteration k (designated by the right-hand subscript). The algorithm is equipped with a line-search regime for determining the step size Δ_k in the parameterized solution

$$\chi_k = \chi_{k-1} + \Delta_k \bar{\chi} \tag{7}$$

where $\Delta_k \bar{\chi}$ is the total change in the estimated parameters from the previous step and χ_k and χ_{k-1} are the current and previous step estimates, respectively, given by the stacked vectors

$$\chi_k = \begin{bmatrix} E_{1,k} \\ E_{2,k} \\ \nu_{12,k} \\ \nu_{21,k} \\ G_{12,k} \end{bmatrix} \text{ and } \chi_{k-1} = \begin{bmatrix} E_{1,k-1} \\ E_{2k-1} \\ \nu_{12,k-1} \\ \varnothing \\ G_{12,k-1} \end{bmatrix}. \tag{8}$$

In this concatenated formulation, we also inscribe the elastic components in χ_k and χ_{k-1} with the subscripts k and $k-1$ to emphasize that they are updated and stored at each iteration. To compute $\bar{\chi}$ we stack the LS updates for each elastic parameter as follows:

§ See [46] for additional details related to the computation of L_χ and Γ_χ.

$$\bar{\chi} = \begin{bmatrix} (J_{E_1,k-1}^T W^{-1} J_{E_1,k-1} + \Gamma_{E_1}^{-1} + H_{c,E_1})^{-1} (J_{E_1,k-1}^T W^{-1}(u_m - U(\chi_{k-1})) - g_{E_1} - g_{c,E_1}) \\ (J_{E_2,k-1}^T W^{-1} J_{E_2,k-1} + \Gamma_{E_2}^{-1} + H_{c,E_2})^{-1} (J_{E_2,k-1}^T W^{-1}(u_m - U(\chi_{k-1})) - g_{E_2} - g_{c,E_2}) \\ (J_{\nu_{12},k-1}^T W^{-1} J_{\nu_{12},k-1} + \Gamma_{\nu_{12}}^{-1} + H_{c,\nu_{12}})^{-1} (J_{\nu_{12},k-1}^T W^{-1}(u_m - U(\chi_{k-1})) - g_{\nu_{12}} - g_{c,\nu_{12}}) \\ \text{Ø} \\ (J_{G_{12},k-1}^T W^{-1} J_{G_{12},k-1} + \Gamma_{G_{12}}^{-1} + H_{c,G_{12}})^{-1} (J_{G_{12},k-1}^T W^{-1}(u_m - U(\chi_{k-1})) - g_{G_{12}} - g_{c,G_{12}}) \end{bmatrix}$$
(9)

where "J" refers to a Jacobian with respect to an estimated elastic property designated in the lower right-hand subscript, for example $J_{E_1,k-1}$ is "the Jacobian with respect to $E_{1,k-1}$." Further details on the computation of J will be provided later in this section. The presence of the placeholder Ø in Eqs. 8 and 9 and the absence of $J_{\nu_{21},k-1}$ in Eq. 9 results from the fact that $\nu_{21,k}$ may be computed using the symmetry of $\mathcal{C}$ with the relation

$$\nu_{21,k} = \nu_{12,k}\frac{E_{2,k}}{E_{1,k}}.$$
(10)

Additionally, the variables g_{c,E_1}, g_{c,E_2}, $g_{c,\nu_{12}}$, and $g_{c,G_{12}}$ are the gradient vectors and H_{c,E_1}, H_{c,E_2}, $H_{c,\nu_{12}}$, and $H_{c,G_{12}}$ are the Hessian matricies computed from the polynomial constraints on χ; the first subscript "c" denotes "constraint" and the following subscript denotes the elastic property. The gradients related to the prior models (cf. Eq. 5), g_{E_1}, g_{E_2}, $g_{\nu_{12}}$, and $g_{G_{12}}$, were computed following [48]. The gradient with respect to $E_{1,k-1}$ would, for example, be computed using

$$g_{E_1} = E_{1,k-1} - E_{1,\exp}\Gamma_{E_1}^T.$$
(11)

As noted previously, the GN approach requires computation of the stacked Jacobian $J_{\chi_{k-1}} = \frac{\partial U}{\partial \chi_{k-1}} = [J_{E_1,k-1}, J_{E_2,k-1}, J_{\nu_{12},k-1}, J_{G_{12},k-1}]^T = [\frac{\partial U}{\partial E_{1,k-1}}, \frac{\partial U}{\partial E_{2,k-1}}, \frac{\partial U}{\partial \nu_{12,k-1}}, \frac{\partial U}{\partial G_{12,k-1}}]^T$ at each iteration k. To compute J_χ, we employ the perturbation method with central differencing following [49]. The computation of $J_{\chi_{k-1}}$ is not trivial. Computing $J_{\chi_{k-1}}$ is the most expensive and time-consuming portion of the proposed algorithm. This is because computing $J_{\chi_{k-1}}$ requires $8N_n + 1$ computations of $U(\chi)$ per iteration. One alternative to the proposed least-squares algorithm is to the adjoint method, as described in [36]. The use of adjoint method in stacked applications will be examined in future works.

3. DIC approach

In this work, we use an iterative Optical Flow/LS approach for determining the displacement field u_m, which serves as an input to the inverse algorithm outlined in the previous section. The DIC approach is modeled after the well-known LS algorithm described in [50]. Broadly speaking, the aim of the DIC algorithm is to map the central coordinates (x_l, y_l) of the reference image subsets to the central coordinates of the deformed image's subsets (x'_l, y'_l).

Assuming a linear change in pixel intensities between grayscale images $\alpha(x_l, y_l)$ and $\beta(x'_l, y'_l)$, we have

$$A\alpha(x_l, y_l) + B = \beta(x'_l, y'_l), \ l = 1, 2, 3 \ldots n \tag{12}$$

where A is an intensity change coefficient and B is an intensity shift and n refers to the number of pixels in the reference subset.

To determine the displacement mapping function, we first write Eq. 12 in terms of the integer pixel displacement components q and v (note: $u_m = [q, \ v]^T$) and the sub-pixel displacement components Δq and Δv

$$x'_l = x_l + q + \Delta q + q_x \Delta x_l + q_y \Delta y_l \tag{13}$$

and

$$y'_l = y_l + v + \Delta v + v_x \Delta x_l + v_y \Delta y_l \tag{14}$$

where the subscripts "x" and "y" denote the parameters' x and y directional components. By substituting Eqs. 13 and 14 into Eq. 12, we obtain

$$\beta(x_l + q + \Delta q + q_x \Delta x_l + q_y \Delta y_l, \ y_l + v + \Delta v + v_x \Delta x_l + v_y \Delta y_l) - A\alpha(x_l, y_l) - B = 0 \tag{15}$$

Taking the Taylor expansion of Eq. 15 about $\beta(x_l + q, y_l + v)$ and collecting only first-order terms, we obtain the following function

$$\pi(p) = \beta + \beta_x \Delta q + \beta_x q_x \Delta x_l + \beta_x q_y \Delta y_l + \beta_y \Delta v + \beta_y v_x \Delta x_l + \beta_y v_y \Delta y_l - A\alpha - B \approx 0 \tag{16}$$

where $p = [\Delta q, \ q_x, \ q_y, \ \Delta v, \ v_x, \ v_y, \ A, \ B]^T$ is a vector of unknown parameters. We may then optimize the function π using an iterative Newton-based scheme

$$\pi(p_k) = \pi(p_{k-1}) + \nabla\pi(p_{k-1})(\pi(p_k) - \pi(p_{k-1})) \leq \text{tol} \tag{17}$$

where p_k is the solution vector at the kth iteration, tol is the stopping criteria and $\pi(p_{k-1})$ is defined by

$$\begin{aligned}
\pi(p_{k-1}) = \ & \beta(x_l + q + \Delta q_{k-1} + q_{x,k-1}\Delta x_l + q_{y,k-1}\Delta y_l, \\
& y_l + v + \Delta v_{k-1} + v_{x,k-1}\Delta x_l + v_{y,k-1}\Delta y_l) - A_{k-1}\alpha(x_l, y_l) - B_{k-1}).
\end{aligned} \tag{18}$$

We may now write the iterative LS solution for p_{k-1} in Eq. 17 as

$$p_k = p_{k-1} - [\nabla\pi(p_{k-1})^T \nabla\pi(p_{k-1})]^{-1} \nabla\pi(p_{k-1})^T \pi(p_{k-1}). \tag{19}$$

The DIC regime was selected for the following reasons: (i) fast minimization of Eq. 17, (ii) the scheme allows for large translations, rotations, shear deformations, and combinations thereof, and (iii) the lack of computing resources required. We remark that, in the case of large rotations, selection of the initial parameter field should be selected with care (cf. [51] for more information).

4. Outline of DIC-QSEI algorithm and computing approach

The algorithm for the joint DIC and QSEI is shown in Figure 1. The flow chart begins with the input of digital images into the DIC algorithm, which outputs the displacement field u_m when the residual is lower than a given tolerance. Following, the displacement fields serve as data inputs for the QSEI regime, which utilizes a GN regime to minimize the cost function, after which the the elastic parameters are recovered. Additional technical details regarding DIC and QSEI are provided in the previous two sections.
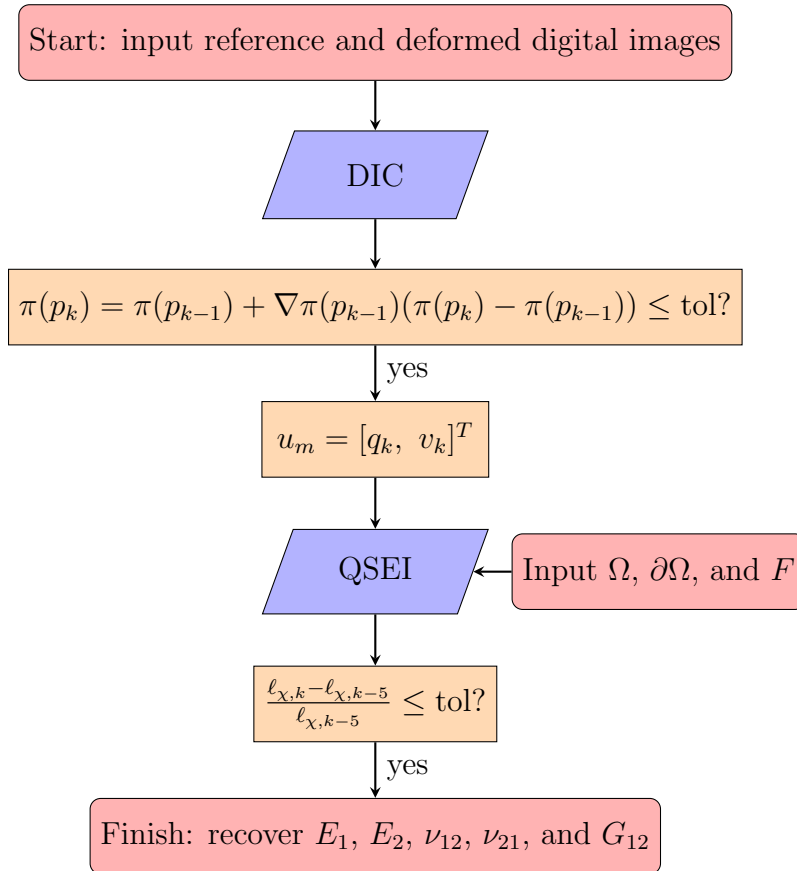

Figure 1. Algorithm outline for DIC/QSEI estimation of orthotropic elastic parameters.

In our computing approach, all computations were executed in a load sharing facility using four quad-core Xeon processors running at 3.3 GHz with 64 Gb of memory allocated. In this work, we computed the four Jacobians (for E_1, E_2, ν_{12}, and G_{12}) in parallel (one on each quad-core processor), since computing the Jacobians consumed the majority of the computational time. For the linesearch and evaluation of the cost function, only one of the quad-core processors was used, since evaluating these are relatively low in computational demand compared to computing the Jacobians.

5. Simulation study

In this section, we test the QSEI algorithm in a controlled setting using noisy simulated DIC displacement data generated from the forward model. We begin by discussing the simulated geometries and simulation conditions. Following, we present the simulation results with discussion and analysis of the QSEI algorithm's performance.

5.1. Simulation geometries and conditions

We begin by generating randomized (blob-like) distributions of E_1, E_2, ν_{12}, and G_{12} and superimposing them on the data-simulation mesh. To simulate experimental conditions, DIC displacement data is obtained using a fine mesh and adding $\eta = 1.0$ and 2.0% noise standard deviation to the data. Following, the data is interpolated onto a coarser inverse mesh using spline interpolation. Three geometries are studied: (i) a stretched plate, (ii) a cantilevered beam in bending, and (iii) a beam in three point bending. The FEM meshes, boundary conditions, and external forces for each case are shown in Figure 2.
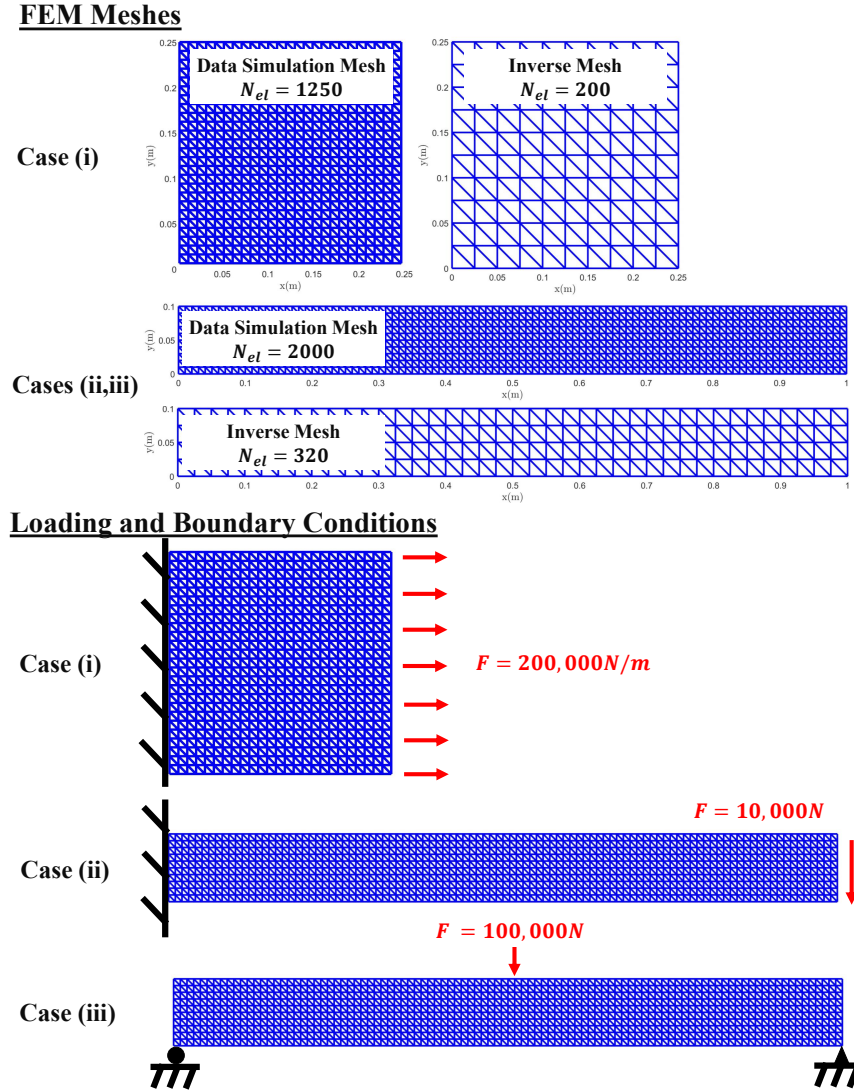
FEM Meshes

Loading and Boundary Conditions

Figure 2. Schematic illustration of structural geometries, loading conditions, boundary conditions, and FEM meshes. Case (i) 0.25 m × 0.25 m stretched plate with fixed left end: 200,000 N/m load evenly distributed among right side nodes, case (ii) 0.1 m × 1 m plate bending with fixed left end: 10,000 N shear load evenly distributed among right side nodes, and case (iii) three-point plate bending with a 100,000 N central point load. Each geometry had a plate thickness of 0.015 m.

The meshing for cases (ii) and (iii) is identical, this choice was made based off available computational resources. We note that the total number of estimated parameters is proportional to the number of elements in the inverse mesh N_{el}. In general, QSEI regimes aim to reconstruct one elastic parameter (usually isotropic E or ν), resulting in $1 \times N_{el}$ unknown parameters. However, here, we aim to reconstruct four elastic parameters, and therefore have $4 \times N_{el}$ unknown parameters. For example, in cases (ii) and (iii) we estimate 1280 elastic parameters. In general, inverse estimation of over 10^3 elastic parameters is computationally demanding [36].

The selection of simulated elastic parameters for this study was done based on representative values available in literature for unidirectional carbon-fiber composites [52–54]. In all cases, the elements are assumed to have uni-directional fibers oriented parallel to the horizontal axis shown in Fig. 2. In preliminary simulation studies, it was found that the reconstruction of randomized inhomogeneous distributions of E_1, E_2, and G_{12} with low variability (for example, less than 10% the magnitude of a homogeneous distribution) was rather straightforward. Since we are interested in reconstructing materials that may have significant inhomogeneity, the variability of parameters E_1, E_2, and G_{12} used were 66% of the homogeneous literature values (e.g., $E_1 = E_{1,\text{homogeneous}} \pm \frac{1}{3}E_{1,\text{homogeneous}}$). For ν_{12}, a total variability of 6.5% was selected; higher variability in ν_{12} resulted in poor performance of the algorithm during preliminary trial runs. The poor performance was caused by three primary factors (i) since ν_{21} is computed as a function of E_1, E_2, and ν_{12} via Eq. 10, no prior information is directly used in modeling its distribution, (ii) ν_{21} was not constrained during minimization, and (iii) compound misestimation in computing ν_{21} before optimized values of E_1, E_2, and ν_{12} are reached. The range of the true elastic parameters used in simulations are reported in Table 1 and shown visually in the following section.

Table 1. Elastic properties used in simulations.

	E_1 (GPa)	E_2 (GPa)	ν_{12} (GPa)	ν_{21} (GPa)	G_{12} (GPa)
Case (i)	300 ± 100	30 ± 10	0.325 ± 0.025	$\nu_{12}\frac{E_2}{E_1}$	45 ± 15
Case (ii)	300 ± 100	30 ± 10	0.325 ± 0.025	$\nu_{12}\frac{E_2}{E_1}$	45 ± 15
Case (iii)	300 ± 100	30 ± 10	0.325 ± 0.025	$\nu_{12}\frac{E_2}{E_1}$	45 ± 15

5.2. Simulation results

5.2.1. Case (i): plate stretching The reconstructions for case (i), are shown in Figure 3 plotted atop the displaced geometries. At both levels of noise, reconstructions well capture the true elastic distributions. At $\eta = 2.0\%$, reconstructions are blurrier than at $\eta = 1.0\%$. Although subtle, this observation is perhaps most clear in the comparison of $E_2(\eta = 2.0\%)$ to $E_2(\eta = 1.0\%)$. Such a result is expected as noise corruption is well known to have a blurring effect on the image quality using QSEI [35].
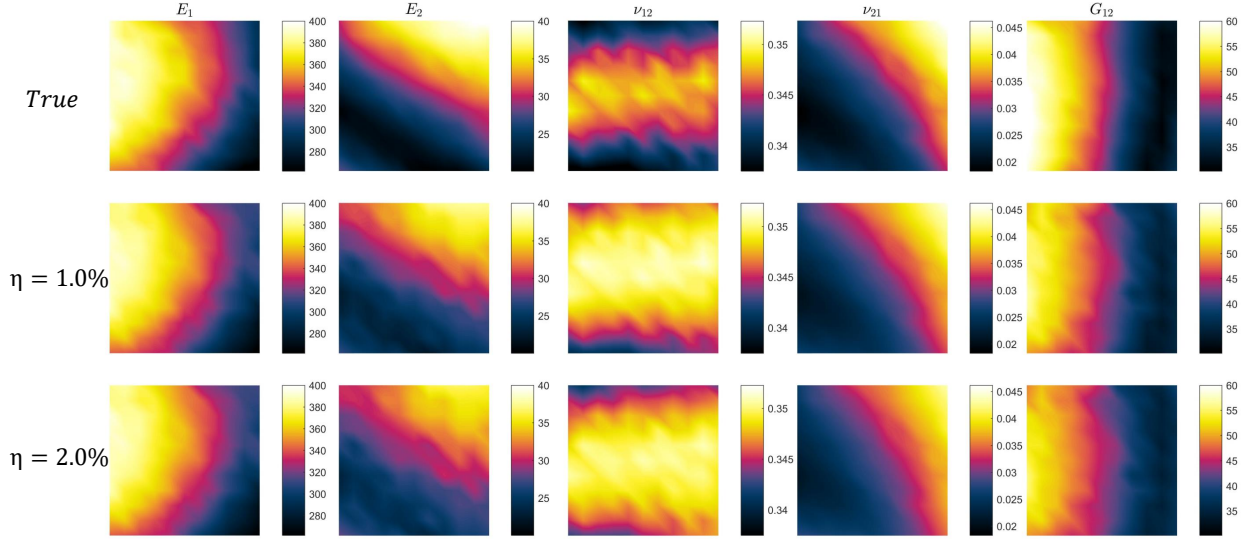
Figure 3. Reconstructions for case (i) plotted atop the displaced geometries. Top row, true distributions of χ; middle row, reconstructed estimates with $\eta = 1.0\%$; bottom row, reconstructed estimates with $\eta = 2.0\%$. Units of E_1, E_2, and G_{12} are in GPa; ν_{12} and ν_{21} are unitless.

Of the estimated parameters, reconstructions of ν_{12} have the largest visual discrepancy with respect to the true distributions. In general, however, ν_{12}, E_2, and ν_{21} estimates are notably higher in magnitude than the true images. This indicates that misestimation of one parameter has a compound effect on the estimation of others. Upon inspection of Eq. 1, it is clear that, in each non-zero entry of $\mathcal{C}$, misestimation of one elastic parameter may be compensated by another constitutively-linked elastic parameter. This realization indicates that high-degree of non-uniqueness in the estimation of Eq. 4. In the discussion portion of the simulation study, we will reanalyze these qualitative visual observations quantitatively.

5.2.2. Cases (ii,iii): plate bending Reconstructions for cases (ii) and (iii) are shown in Figure 4 plotted atop the displaced geometries. We again observe that, in general, the true distributions of the elastic properties are captured in the QSEI reconstructions. It is clear, however, that the reconstructions in plate bending (i) compare less favorably to true images than the plate stretching reconstructions and (ii) are more sensitive to added noise.
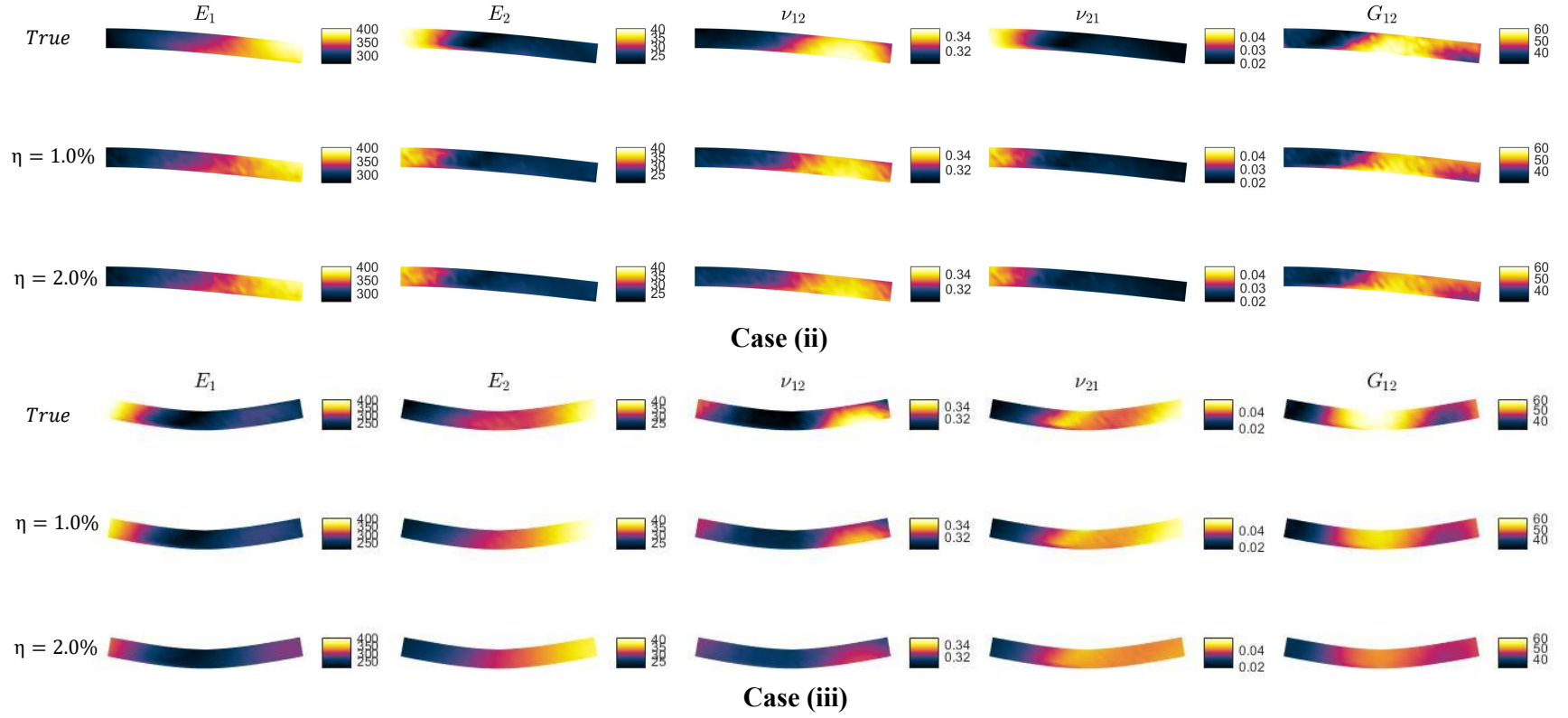
Figure 4. Reconstructions for cases (ii,iii) plotted atop the displaced geometries. For each case: top row, true distributions of χ; middle row, reconstructed estimates with $\eta = 1.0\%$; bottom row, reconstructed estimates with $\eta = 2.0\%$. Units of E_1, E_2, and G_{12} are in GPa; ν_{12} and ν_{21} are unitless.

A primary contributor to the decreased quality of plate bending reconstructions is influence of boundary conditions. Upon inspection of Figure 2, we observe that the ratio of constrained nodes to degrees of freedom is much higher for case (i) than cases (ii) and (iii). The added constraints significantly affect the local deformation fields (decrease smoothness) and incorporate prior information into the solution regime via $\partial\Omega$. It is interesting to note that, although reconstruction quality is generally considered to be proportional to the magnitude of the measured field [42, 46, 55], the effect of boundary constraints appears to more significantly effect reconstruction quality (note the magnitude of bending vs. plate stretching displacements). Further supporting this realization: case (ii) has a higher ratio of constrained nodes to degrees of freedom than case (iii), which is reflected in the increased quality of case (ii) reconstructions relative to case (iii).

As a whole, case (iii) reconstructions are notably smoother than case (ii) reconstructions. Moreover, compounding effects and compensation of constitutively-linked elastic parameters are more evident in case (iii) than case (ii). Indeed, localized peaks and valleys in case (iii) estimations ν_{12} and G_{12} are not well reconstructed, especially at $\eta=2.0\%$. We remark again, that these observations are based off visual observation and require quantification, which is provided in the following section.

5.3. Discussion of simulation results

5.3.1. Quantitative analysis of reconstructed images from simulated data

In the previous subsections, it was shown that the proposed QSEI approach captured the true distributions of elastic properties. As a whole, visual observations indicated that the presence of increasing noise blurred and diminished reconstruction quality. Moreover, it was claimed that the plate-stretching reconstructions provided the most accurate estimation of elastic parameters, followed successively by cantilever and three point plate bending. Here, we aim to quantify these observations by computing the root mean square error for each estimated quantity. For example, the RMSE for E_1 is calculated using

$$\text{RMSE}(\text{E}_1) = \sqrt{\frac{\sum_{l=1}^{N_{el}}(\widehat{E}_{1,\text{true}} - E_{1,\text{inverse}})^2}{N_{el}}} \tag{20}$$

where $\widehat{E}_{1,\text{true}}$ are the true elasticity moduli interpolated onto the coarse mesh with the same spline functional used to interpolate simulated DIC data onto the inverse mesh.

The RMSEs for cases (i-iii) are shown in Figure 5. Results from Figure 5 confirm the visual observations from the previous subsections. Based off these results, we may conclude that (a) higher noise increased the RMSE for each estimated parameter, (b) estimates of E_1, E_2, ν_{12}, and G_{12} were most accurately reconstructed in case (i) and most poorly reconstructed in case (iii), and (c) estimation of ν_{21} did not follow the trend noted in (b) due to compounded errors in estimating E_1, E_2, and ν_{12}.
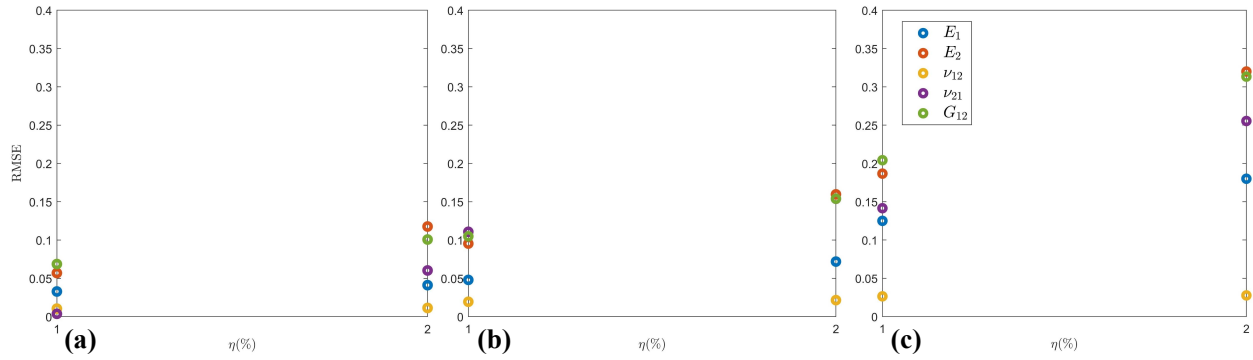
Figure 5. Computed RMSEs for all estimated parameters: (a) case (i), plate stretching; (b) case (ii), cantilever plate bending; (c) case (iii), three-point plate bending. The x-axis is labeled with the the noise level η, which is 1.0% or 2.0%.

There are numerous contributors influencing the RMSEs and quality of reconstructions in this simulation study, including geometrical, numerical, and material factors. In the following list, we highlight key sources affecting the reconstructions and providing a brief discussion of each (cause : effect).

- Noise: increasing random noise increased RMSE and decreased reconstruction quality.

- Interpolation error: interpolating noisy data from the fine simulation mesh to the coarse inverse mesh decreased reconstruction quality.

- Discretization error: increases RMSE and decreases reconstruction quality. Described in detail in [48], the criticality of discretization errors scales with the size of the inverse problem.

- Boundary conditions/constraints: increasing boundary constraints improved reconstruction quality. This was particularly clear in case (i), where (a) the ratio of constrained nodes to total degrees of freedom was the highest and (b) RMSE was the lowest.

- Distribution of material properties: can have a positive or negative effect on reconstruction quality. Significant fluctuations of χ in areas of high sensitivity are preferred to high fluctuations of χ in areas of low sensitivity. Although, "areas of high-sensitivity" is not well defined in literature, we broadly deduce that "high sensitivity areas" have the following attributes based off general principles of inverse problems: (a) high signal-to-noise ratio, i.e. large measured displacements u_m and (b) information related to localized deformation fields, such as large displacement gradients ∇u_m.

- Prior models for χ: accurate prior models are essential. In this case, we have prior knowledge that distributions of χ are smooth, therefore we use smoothness-promoting regularization instead of, for example, TV- or L_1-based regularization which promote sparsity and may result in reconstructions that do not represent the problem physics well.

- Physically-realistic constraints on χ: improve reconstruction quality. The constraints on χ are required to ensure the parameters are within physically-realistic limits, resulting in realistic solutions. Preliminary simulation results indicate that the constraint $E_1 > E_2$ was critical in obtaining accurate estimates of E_2 and G_{12}.

- Jacobian estimation: poor estimation of J_χ decreases reconstruction quality or may lead to minimization of Eq. 4 in the wrong direction. Although first-order central differencing was satisfactory for reconstructions herein, reconstruction quality can be improved using higher order estimations of J_χ (at the cost of computational time). In preliminary studies, lower-order estimation of J_χ, using forward or backwards differencing, generally resulted in poor reconstruction quality.

5.3.2. Analysis of computations

In this subsection, we aim to gain additional insights into the behavior of the proposed QSEI regime by analyzing the computations. Of practical importance, we begin by providing the computing time for each of the six QSEI reconstructions using simulated data. To do this, we have tabulated the total number of iterations, total computing time, and average computing time per iteration in Table 2.

Table 2. Computational performance of the proposed QSEI regime

Reconstruction	Iterations k	Total Computing Time (min)	Time/Iteration (min)
Plate Stretching ($\eta = 1\%$)	21	126.52	6.03
Plate Stretching ($\eta = 2\%$)	30	177.28	5.91
Cantilever Beam ($\eta = 1\%$)	26	236.60	9.10
Cantilever Beam ($\eta = 2\%$)	30	288.33	9.61
3-Point Beam ($\eta = 1\%$)	29	264.98	9.14
3-Point Beam ($\eta = 2\%$)	30	276.60	9.22

From Table 2, we observe that all reconstructions reached the stopping criteria between 20 and 30 iterations. In every case, the number of iterations for $\eta = 2\%$ was highest. This may result from the relative infeasibility of the prior models. Indeed, in a rough sense, we may consider that the weights of L_χ and L_e result in a relative tradeoff between the resolution and noise attenuation in the reconstructed images. One way of improving the algorithm's performance is to adaptively select regularization/weighting parameters at each iteration.

On the other hand, we observe from Table 2 that the total computing times scaled linearly with the number of iterations and the mesh density, which is anticipated since none of the computations (evaluation of the forward model, objective function, and Jacobian) are dependent on the noise level. We do note, that the computation of the Jacobian amounted to approximately 90% of the total computation times and is the major computational disadvantage of this regime. What is not apparent in Table 2, however, is the minimization behavior of the objective function (Eq. 4) throughout the iterations. This behavior,

quantified in terms of the relative objective function drop at each iteration, is shown in Fig. 6 for all the simulation cases.
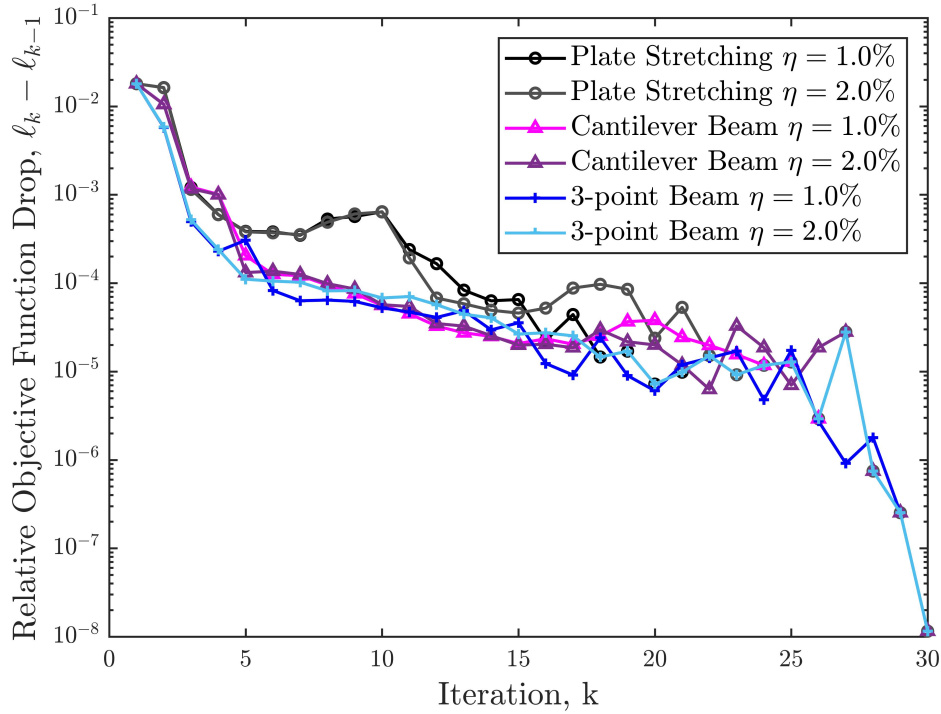

Figure 6. Relative drop in the objective function ℓ at each iteration k.

Fig. 6 shows similar behaviors in the relative drops and rates of relative drops between objective functions. Indeed, in all cases, the drops in the objective functions generally become smaller as the iteration number increases. This is a common feature of Jacobian-based LS optimization regimes – large initial decreases in the objective function values and gradual flattening as iterations increase. One subtle difference, however, is observed in the initial behavior of the plate stretching in comparison with the bending cases; that is, the large initial relative drops for plate stretching cases are sustained for longer. This may result from the more uniform global sensitivity of plate stretching to changes in χ, which manifested in larger drops of the objective function and lower RMSE values (as observed in the previous section) relative to the bending cases.

6. Experimental program

In this section, we utilize DIC to obtain the displacement fields from three-point bending tests of uni-directional CFRP beams. Using the DIC data, we aim to reconstruct images of damaged and undamaged specimens by employing the QSEI algorithm proposed herein. We begin by detailing the experimental program. Following, we present the reconstructions using experimental data and provide a discussion of the results.

6.1. Experimental setup

Experimental validation of the QSEI algorithm was conducted using quasi-static three-point bending of pultruded CFRP beams. A total of three samples were tested: case (a), undamaged sample; case (b), sample with localized damage 25.0 mm left of center; and case (c), sample with localized damage 25.0 mm right of center. Flat-bottomed holes were drilled off-center in order to artificially generate a local deviation in stiffness as outlined in [56]. The diameter and depth of the holes were determined using optical microscopy and the expected drop in flexural rigidity due to reduction in cross-section area was determined using CAD software. The bending setup was constructed following ISO 14125 guidelines [57]. A span-to-thickness ratio of 40 was selected to ensure the beam deformations were primarily bending with small shear forces in comparison. This allowed for large displacement fields without significant localized damage near the supports and externally-applied load. It should be noted that the roller diameter used is larger than the 6 mm diameter recommended by ISO14125 [57]. This mainly affects the effective span under large deflection conditions [58]. This effect was mitigated by limiting the maximum deflections to approximately 5.0 mm (further discussed in the following section).

The selected experimental boundary conditions were pinned-fixed (left support–right support). The right support cylinder was fitted with coarse-grit sandpaper to ensure a fixed condition whereas the left support and the loading nose were lubricated to allow free movement in the horizontal direction. The speed of testing was 3.0 mm/min and force, time and cross-head displacement were recorded during the tests. The experimental setup is shown in Figure 7.
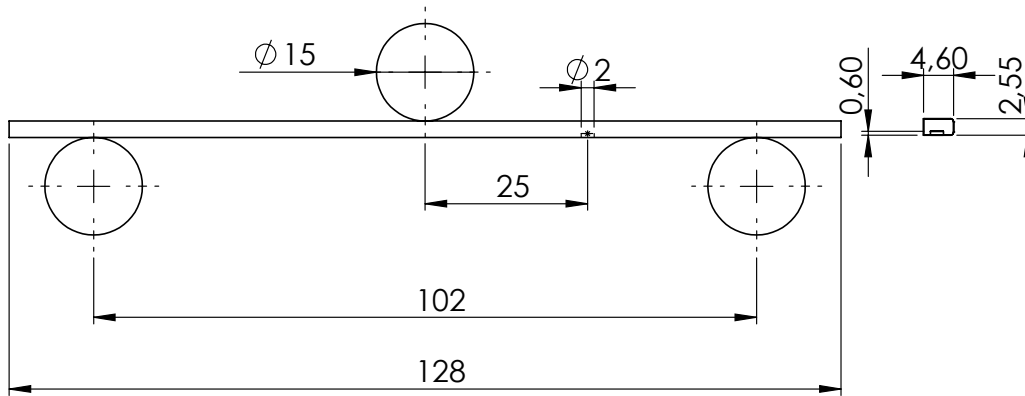

Figure 7. Three-point bending setup with sample and right-side defect dimensions (dimensions in mm).

One face of the CFRP beam was sanded to produce a planar surface from top to bottom of the beam. Otherwise, the corner fillets typically present in pultruded rods would make

the edges difficult to image. The corner fillets on the backside were not sanded in order to avoid breaking fibers and to minimize possible variations in the beam cross-section. The analytically calculated second moment of area I_{xx} with a 0.5 mm radius fillet on the backside is 1.8% smaller than the approximation of a rectangular cross-section with sharp corners ($I_{xx} = \frac{bh^3}{12}$). It should be noted that the measured flexural stiffness is slightly lower than the theoretical (rectangular) value since the effects of the corner fillets were neglected in the analysis.

To obtain the DIC displacement field, a white speckle pattern was air-brushed on the sanded beam surface to provide a contrast pattern. An example image of a displaced beam with an applied DIC contrast pattern is shown in Figure 8 within the experimental setup. A Basler acA2000-340km camera with 2048 pixel × 1088 pixel resolution was used to record images of the side of the beam during bending. In the DIC computational approach, we utilized a subset size of 11 × 11 pixels. The selection of the subset size was was determined based on an ad hoc process aiming to obtain ample displacement resolution to clearly distinguish displacement gradients near the hole location. This process resulted in a total of 1,070 subsets enclosing the beam geometry each containing approximately 2-4 speckles, where a square with a side length of approximately 3-5 pixels was found to be adequate to resolve an average-sized speckle. This regime which was found to be satisfactory for the small displacement fields.
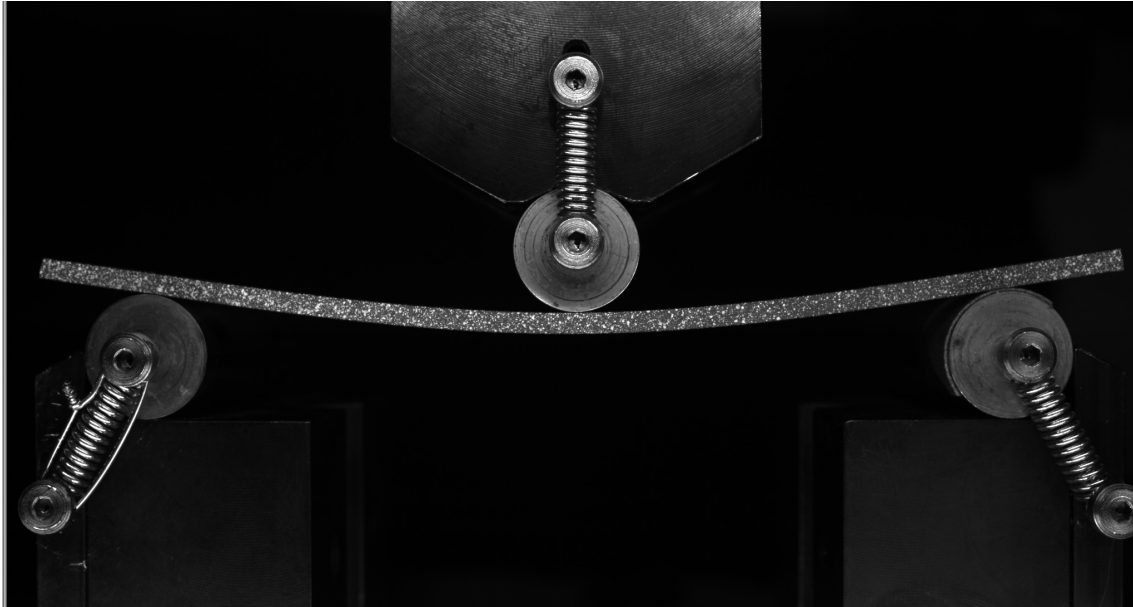

Figure 8. Example image of a displaced beam with sprayed DIC contrast pattern in experimental conditions.

Elastic properties (assumed to be homogeneous) of the composite material were measured for comparing with the QSEI reconstructions. E_1 and ν_{12} were measured using a uniaxial tensile test with strain gauges bonded parallel and perpendicular to fiber direction,

following the procedures in ISO527-5 [59]. E_1 was calculated using linear regression of the stress-strain data in the strain interval 0.0005-0.0025. ν_{12} was measured as a function of strain, where the accepted value was taken after stabilization. E_2 was obtained using micro-DIC in transverse compression. The cross-section of the beam was polished and the fibers themselves were used as a contrast pattern. A specimen was compressed between two steel discs and strain was measured using DIC and a virtual strain gauge in DaVis software by LaVision GmbH.

While homogeneous estimation of E_1, E_2, ν_{12}, and ν_{21} (via Eq. 10) is rather straight forward, G_{12} is difficult to measure experimentally [60]. Therefore a literature value for a similar unidirectional carbon fiber composite was utilized [5]. It is unclear, however, how the experimental shear modulus values were obtained in the literature estimate. Analytical equations by Chamis [3] were also used with the fiber and resin values provided to us by the manufacturer of the CFRP rod, but it is unclear how the shear modulus of the fiber was measured. Using these methods we obtain values for G_{12} in the range of 4.7-7.6 GPa ($\approx 6.0 \pm 2.0$ GPa). A summary of the composite material elastic properties is presented in Table 3

Table 3. Homogeneous elastic properties based on experimental data and literature estimates.

	E_1 (GPa)	E_2 (GPa)	ν_{12} (GPa)	G_{12} (GPa)
Method	Tensile test	Transverse compression	Tensile test	Literature and analytical
Value	148.0	7.0	0.29	6.0 ± 2.0

6.2. DIC-QSEI imaging

The DIC algorithm presented in section 3 was used to determine the displacement field of the composite beams. For each case (cf. section 6.1 for details), two photographs were used in the DIC algorithm, a reference image (before loading) and the displaced-beam image. For the displaced-beam images, photographs meeting following criteria were prescribed (i) the beams are required to be below the limit of large vertical displacements and (ii) no damage is observed in the load-displacement curves. Criteria (i) was computed using $\frac{L}{10} = 10.2$ cm, following [58]. Ten times the span is also considered the limit for linear behavior in [57]. By inspecting the load-displacement curves, the criteria for the limiting point force F_m was conservatively determined to be $F_m = 150$ N. The limiting force corresponded to a displacement of approximately 5.0 mm for all beams and was therefore the controlling criteria.

Images taken at F_m and images from the reference configurations were analyzed to obtain the DIC displacement field. The DIC displacement fields were then interpolated using spline interpolation onto the QSEI mesh; these displacement fields u_m were then used in the minimization of Eq. 4 following the regime outlined in Figure 4. The QSEI mesh consisted of $N_{el} = 1632$ triangular elements with a maximum dimension of 0.75 mm. This mesh

was selected based on available computational resources and the desired resolution of the reconstructions; in this study, the desirable maximum element dimension was less than the radii of the localized damages. An example of a displaced QSEI mesh is shown in Figure 9.
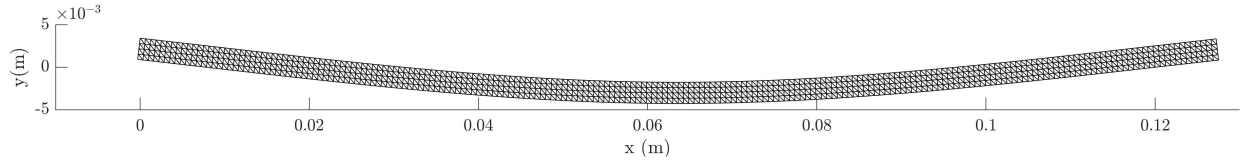

Figure 9. Example of a displaced QSEI grid using an interpolated displacement field obtained using DIC.

Reconstructions of χ for cases (a-c) are shown in Figure 10. In general, estimations of χ in the undamaged beam are relatively homogeneous and in agreement with values provided in section 6.1. The homogeneity of the images is expected since the fibers are evenly distributed and uni-directional. One possible deviation is the estimation of G_{12}, which is significantly different than values provided in Table 3. We would like to remark, however, that homogeneous literature and computed values of G_{12} are decidedly varied and do not use the same fiber material as the material tested here. Furthermore, the analytical micro-mechanical solutions vary greatly when transverse properties are involved [61]. It is therefore difficult to determine if the differences in G_{12} estimated herein are in significant error.
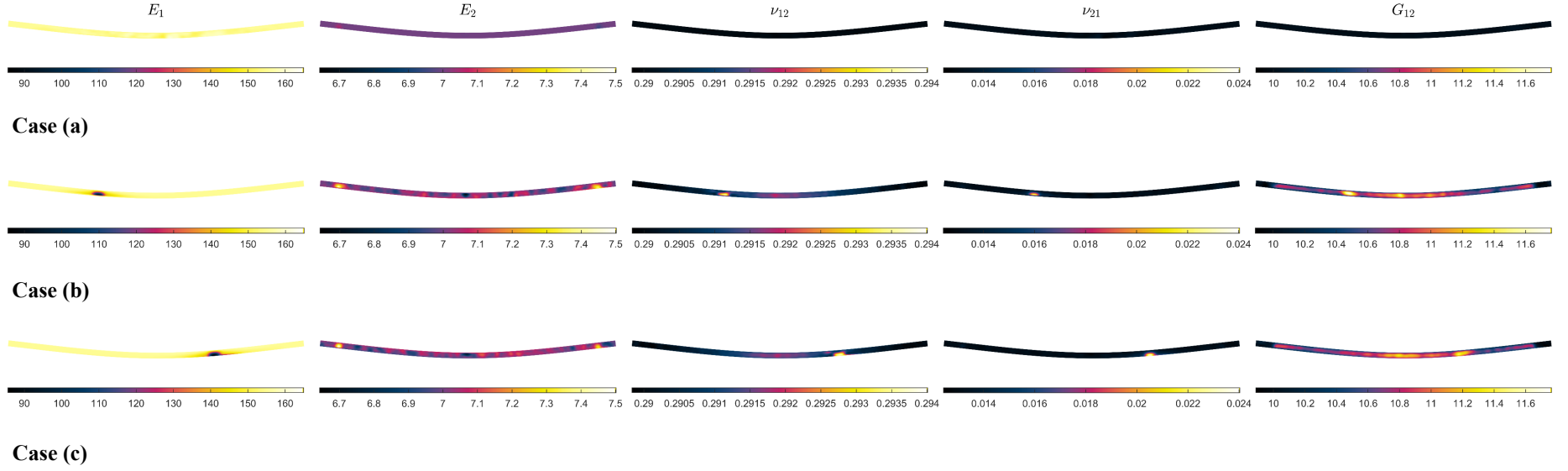
Figure 10. Reconstructions of χ for cases (a-c) plotted atop the displaced geometries of uni-directional composite beams. Case (a), undamaged beam; case (b) beam with localized damage on the left hand side; and case (c) beam with localized damage on the right hand side. Units of E_1, E_2, and G_{12} are in GPa; ν_{12} and ν_{21} are unitless.

Images of cases (b) and (c) clearly show the localized damages in reconstructions of E_1, ν_{12}, and ν_{21}. The damaged locations are most distinct in reconstructions of E_1. This is an expected result, since the properties and orientation of the reinforcement fibers are the primary contributor of the beams' bending stiffness and therefore E_1 has the largest effect on the measured displacement field. In addition, the method presented here provides a quantitative measure of the local stiffness, which can be used to estimate the extent of damage. The reduction in flexural rigidity due to the artificial defects is calculated to be 25% and a similar drop is seen in E_1. In the case of ν_{12} and ν_{21}, we observe local increases in the areas of damage. This indicates that the damaged regions have become more complaint in the directions parallel and perpendicular to the direction of bending stresses. Such an observation is consistent with the fact that the damaged region is locally less stiff than surrounding regions.

On the other hand, reconstructions of E_2 and G_{12} do not discernibly localize damage. There are two possible explanations for this, which are highlighted as follows. Firstly, E_2 and G_{12} significantly affect transverse deformations; however, since this beam is very slender, perturbations in these parameters are difficult to capture in the measured displacement fields. Secondly, cross-talk between parameters E_2, ν_{12}, and G_{12} due to the non-uniqueness of the inverse problem (cf. the discussions in section 5.2) may have had a mutual effect on the accuracy of each reconstruction. Cross-talk may be mitigated using more precise constraints based off knowledge of the material properties and/or physical realizations [49].

As a whole, reconstruction errors using experimental data may result from a number of the points highlighted in section 5.3. Of particular practical importance are the interpolation of DIC displacement data onto the QSEI mesh and the handling of noise statistics in Eq. 9. In cases where precise information related to transverse deformations are required (i.e. in accurate estimation of E_2 and G_{12}), high-degree polynomial or spline interpolation are recommended. In preliminary analysis, it was found the linear or quadratic interpolation were insufficient, often leading to large fluctuations in E_2 and G_{12} due to errors in the interpolated values of u_m. Indeed, the high sensitivity of E_2 and G_{12} to u_m are observed near the supports, where there are significant contact strains. Moreover, the noise statistics in this work were assumed to be Gaussian. While this assumption was adequate for this work in a controlled laboratory setting, it may not be sufficient all cases where DIC data is used. For example, camera translation or rotation in field applications may result in systematic or skew-symmetric noise statistics significantly corrupting the QSEI algorithms assuming only Gaussian noise statistics.

To summarize, the results presented in the section demonstrate the experimental feasibility of the proposed QSEI/DIC algorithm for simultaneous reconstruction of inhomogenous orthotropic elastic properties in both damaged and undamaged states. In cases with more uncertainty in DIC measurements, future research is required to improve the algorithm's performance with respect to (i) cross-talk between estimated parameters and (ii) the handling of noise statistics.

7. Conclusions

Accurate determination of orthotropic properties is important in the design and health assessment of composite structures. In the present contribution to this field, we propose a regime for simultaneously reconstructing inhomogeneous orthotropic elastic properties. Possible applications include damage detection, materials characterization, and state estimation. The algorithm is based on concepts from Quasi-Static Elasticity Imaging (QSEI), utilizing displacement fields obtained from Digital Image Correlation (DIC). We begin by providing the technical background for QSEI and DIC. Following, the algorithm is tested in a simulation study, where various structural geometries, boundary conditions, and loading conditions ar analyzed. Lastly, we experimentally investigate three-point bending of unidirectional composites with and without localized damage.

The results support the feasibility of the coupled QSEI/DIC regime for reconstructing inhomogeneous elastic properties with or without the presence of localized damage. Simulations results for in-plane plate bending and stretching show that reconstructions of significant inhomogeneity in all orthotropic properties are possible in the presence of random noise and interpolation errors. In the experimental program, estimation of undamaged elastic material properties and damage localization are demonstrated in three-point bending of unidirectional CFRP beams. The quantitative information gained is valuable in engineering applications for two reasons. Firstly, all of the elastic constants of the undamaged material are needed for structural finite element models. Secondly, the results of damaged beams can be directly used for simulating post-damage performance of a component without having to specify damage morphology in the model. More research is needed to confirm the detection capabilities of realistic and distributed damage types. In field applications, with more uncertainty in DIC measurements, additional research is required to improve the algorithm's robustness to (i) cross-talk between estimated parameters and (ii) the handling of non-Gaussian noise statistics.

References

[1] Yoon Y, Yang G and Cowin S 2002 *Biomechanics and modeling in mechanobiology* **1** 83–93
[2] Surana K S 2016 *Advanced mechanics of continua* (CRC Press)

[3] Chamis C C 1983 Simplified composite micromechanics equations for hygral, thermal and mechanical properties NASA technical memorandum 83320 Lewis Research Center, Cleveland, Ohio prepared for the 38th Annual Conference of the Society of the Plastics Industry (SPI)

[4] Reddy J N 2004 *Mechanics of laminated composite plates and shells: theory and analysis* (CRC press)

[5] Sun C and Vaidya R 1996 *Composite Science and Technology* **56** 171–179 ISSN 0266-3538

[6] Chakraborty D, Chakraborty D and Murthy K 2017 *Composite Structures* **160** 185–194

[7] Chakraborty D, Murthy K and Chakraborty D 2014 *Engineering Fracture Mechanics* **124** 142–154

[8] Xavier J, De Jesus A, Morais J and Pinto J 2012 *Construction and Building Materials* **26** 207–215

[9] Flament C, Salvia M, Berthel B and Crosland G 2016 *Journal of Composite Materials* **50** 1989–1996

[10] Tweten D J, Okamoto R J, Schmidt J L, Garbow J R and Bayly P V 2015 *Journal of Biomechanics* **48** 4002–4009

[11] Lasn K, Klauson A, Chati F and Décultot D 2011 *Mechanics of Composite Materials* **47** 435

[12] Tallman T N and Wang K 2016 *Structural Health Monitoring* **15** 235–244

[13] Huether J, Rupp P, Kohlschreiber I and Weidenmann K A 2017 *Measurement Science and Technology*

[14] Orell O, Vuorinen J, Jokinen J, Kettunen H, Hytönen P, Turunen J and Kanerva M 2018 *Composite Structures* **185** 176–185

[15] Koohbor B, Mallon S, Kidane A and Sutton M A 2014 *Composites: Part B* **66** 388–399 ISSN 1359-8368

[16] Brynk T, Molak R M, Janiszewska M and Pakiela Z 2012 *Computational Materials Science* **64** 157–161 ISSN 0927-0256

[17] Carne T G and Wolf Jr J 1979 Identification of the elastic constants for composites using modal analysis Tech. rep. Sandia Labs., Albuquerque, NM (USA); General Motors Research Labs., Warren, MI (USA)

[18] De Wilde W, Sol H and Van Overmeire M 1986 Coupling of lagrange interpolation, modal analysis and sensitivity analysis in the determination of anisotropic plate rigidities *Proceedings of the 4th International Modal Analysis Conference* vol 1058

[19] Deobald L R and Gibson R F 1988 *Journal of Sound and Vibration* **124** 269–283

[20] Lai T and Ip K 1996 *Composite Structures* **34** 29–42

[21] Moussu F and Nivoit M 1993 *Journal of Sound and Vibration* **165** 149–163

[22] Shi Y, Sol H and Hua H 2006 *Journal of Sound and Vibration* **290** 1234–1255

[23] Shi Y, Sol H and Hua H 2005 *Journal of Sound and Vibration* **285** 425–442

[24] Liu G, Lam K and Han X 2002 *Journal of Sound and Vibration* **252** 239–259

[25] Mathieu F, Leclerc H, Hild F and Roux S 2015 *Experimental Mechanics* **55** 105–119

[26] Avril S, Bonnet M, Bretelle A S, Grédiac M, Hild F, Ienny P, Latourte F, Lemosse D, Pagano S, Pagnacco E *et al.* 2008 *Experimental Mechanics* **48** 381

[27] Hild F and Roux S 2006 *Strain* **42** 69–80

[28] Li X, Xi L, Jiang R, Yao L and Jiang H 2011 *Biomedical optics express* **2** 2348–2353

[29] Xu C, Kumavor P D, Aguirre A and Zhu Q 2012 *Journal of biomedical optics* **17** 061213

[30] Karageorghis A, Lesnic D and Marin L 2016 *Computers and Structures* **166** 51–59

[31] Moussawi A, Lubineau G, Florentin E and Blaysat B 2013 *Computer Methods in Applied Mechanics and Engineering* **265** 1–14

[32] Bonnet M and Constantinescu A 2005 *Inverse Problems* **21** R1

[33] Babaniyi O A, Oberai A A and Barbone P E 2017 *Inverse Problems in Science and Engineering* **25** 326–362

[34] Goenezen S, Barbone P and Oberai A A 2011 *Computer Methods in Applied Mechanics and Engineering* **200** 1406–1420

[35] Gokhale N H, Barbone P E and Oberai A A 2008 *Inverse Problems* **24** 045010

[36] Oberai A A, Gokhale N H and Feijóo G R 2003 *Inverse Problems* **19** 297

[37] Kallel F and Bertrand M 1996 *IEEE Transactions on Medical Imaging* **15** 299–313

[38] Liu D, Kolehmainen V, Siltanen S, Laukkanen A and Seppänen A 2015 *Inverse Problems and Imaging* **9(1)** 211–229

[39] Toivanen J, Kolehmainen V, Tarvainen T, Orlande H and Kaipio J 2012 *International Journal of Heat*

    and Mass Transfer **55** 7958–7968

[40] Surana K S and Reddy J N 2016 *The finite element method for boundary value problems: mathematics and computations* (CRC press)

[41] Surana K S and Reddy J N 2017 *The Finite Element Method for Initial Value Problems: Mathematics and Computations* (CRC Press)

[42] Mueller J L and Siltanen S 2012 *Linear and nonlinear inverse problems with practical applications* (SIAM)

[43] Richards M S, Barbone P E and Oberai A A 2009 *Physics in Medicine and Biology* **54** 757

[44] Seppänen A, Hallaji M and Pour-Ghaz M 2017 *Structural Health Monitoring* **16** 215–224

[45] Hallaji M, Seppänen A and Pour-Ghaz M 2014 *Smart Materials and Structures* **23** 085001

[46] Kaipio J and Somersalo E 2006 *Statistical and computational inverse problems* vol 160 (Springer Science & Business Media)

[47] Mei Y, Kuznetsov S and Goenezen S 2016 *Journal of Applied Mechanics* **83** 031001

[48] Kaipio J and Somersalo E 2007 *Journal of Computational and Applied Mathematics* **198** 493–504

[49] Smyl D, Bossuyt S and Liu D Submitted, 2018 *Journal of Engineering Mechanics*

[50] Pan B, Asundi A, Xie H and Gao J 2009 *Optics and Lasers in Engineering* **47** 865–874

[51] Pan B, Xie H m, Xia Y and Wang Q 2009 *Acta Optica Sinica* **29** 400–406

[52] Qiao Y, Bisagni C and Bai Y 2017 *Composites Part B: Engineering* **124** 190–206

[53] Gibson R F 2016 *Principles of composite material mechanics* (CRC press)

[54] Gay D 2014 *Composite materials: design and applications* (CRC press)

[55] Isaacson D 1986 *IEEE transactions on medical imaging* **5** 91–95

[56] Antin K N, Harhanen L and Bossuyt S 2016 Damage detection in CFRP components using DIC *Advancement of Optical Methods in Experimental Mechanics* (*Conference Proceedings of the Society for Experimental Mechanics* vol 3) ed et al J H (Springer) pp 57–62 ISBN 978-3-319-22445-9

[57] 1998 ISO 14125. Fibre-reinforced plastic composites. Determination of flexural properties.

[58] Batista M 2015 *International Journal of Non-linear Mechanics* **69** 84–92 ISSN 0020-7462

[59] 2009 ISO 527. Plastics. Determination of tensile properties. Part 5: Test conditions for unidirectional fibre-reinforced plastic composites

[60] 2002 *Composite materials handbook MIL-HDBK-17-1F. Volume 1. Polymer matrix composites guidelines for characterization of structural materials. Department of Defense.*

[61] Maurin R, Davies P and Baral N 2008 *Applied Composite Materials* **15** 61–73